Metal-insulator transition in monolayer MoS_2 via contactless chemical doping

2D Materials

PAPER

Metal-insulator transition in monolayer MoS_2 via contactless chemical doping

Camiel van Efferen[1,4,*], Clifford Murray[1,4], Jeison Fischer[1], Carsten Busse[2,5], Hannu-Pekka Komsa[3], Thomas Michely[1] and Wouter Jolie[1]

[1] II. Physikalisches Institut, Universität zu Köln, Zülpicher Straße 77, Köln, 50937, Germany
[2] Institut für Materialphysik, Westfälische Wilhelms-Universität Münster, Wilhelm-Klemm-Straße 10, 48149 Münster, Germany
[3] Faculty of Information Technology and Electrical Engineering, University of Oulu, Pentti Kaiteran Katu 1, 90014 Oulu, Finland
[4] These authors contributed equally to this work.
[5] Present address: Department Physik, Universität Siegen, Walter-Flex-Str. 3, 57068 Siegen, Germany.
[*] Author to whom any correspondence should be addressed.

E-mail: efferen@ph2.uni-koeln.de

Keywords: metal–insulator transition, contactless doping, monolayer MoS_2, graphene substrate, density-functional theory, scanning tunneling microscopy/spectroscopy

Supplementary material for this article is available online

OPEN ACCESS

RECEIVED
20 December 2021

REVISED
3 March 2022

ACCEPTED FOR PUBLICATION
11 March 2022

PUBLISHED
28 March 2022

Abstract

Much effort has been made to modify the properties of transition metal dichalcogenide layers via their environment as a route to new functionalization. However, it remains a challenge to induce large electronic changes without chemically altering the layer or compromising its two-dimensionality. Here, a non-invasive technique is used to shift the chemical potential of monolayer MoS_2 through p- and n-type doping of graphene (Gr), which remains a well-decoupled 2D substrate. With the intercalation of oxygen (O) under Gr, a nearly rigid Fermi level shift of 0.45 eV in MoS_2 is demonstrated, whereas the intercalation of europium (Eu) induces a metal–insulator transition in MoS_2, accompanied by a giant band gap reduction of 0.67 eV. Additionally, the effect of the substrate charge on 1D states within MoS_2 mirror-twin boundaries (MTBs) is explored. It is found that the 1D nature of the MTB states is not compromised, even when MoS_2 is made metallic. Furthermore, with the periodicity of the 1D states dependent on substrate-induced charging and depletion, the boundaries serve as chemical potential sensors functional up to room temperature.

Metallic transition metal dichalcogenide (TMDC) monolayers show a plethora of many-body phenomena, such as charge density wave order [1], Mott insulating states [2] or superconductivity [3]. Understanding these correlated phases, as well as their dependence on external electric or magnetic fields, allows the creation of devices with tunable phase transitions [4]. While intrinsic TMDC metals are being extensively investigated, less is known about the metallic properties of intrinsic TMDC semiconductors such as MoS_2 and WS_2, mainly due to experimental difficulties in shifting the chemical potential close to the conduction or valence band.

Monolayer MoS_2 and WS_2 have electronic band gaps of more than 2.0 eV when resting on weakly interacting substrates (see [5] for a discussion of substrate-induced band gap variability in MoS_2). Hence, back-gated devices are typically unable to bring the chemical potential close to the onset of the conduction or valence band before breakdown occurs [6, 7]. Larger shifts are obtained with ionic-liquid-gating. With this method, transport measurements showed that MoS_2 and WS_2 become superconducting when the chemical potential lies within the conduction band [8–13]. However, ionic-liquid-gating suffers from charge inhomogeneities [14]. At low temperatures this effect is exacerbated due to freezing of the liquid [15, 16]. The liquid also hampers complementary measurements using surface sensitive techniques. As a consequence, many open questions remain on the nature of the superconducting dome in MoS_2 [8–10, 17, 18] and WS_2 [12], the origin of the finite density of states within the superconducting gap [19], and on the properties of the (quasi-) metallic phase in between the insulating and superconducting phases [12].

Another method to obtain large shifts of the chemical potential is the introduction of foreign species. This is done through adsorption, elemental substitution or via intercalation between the 2D sheet and its substrate [20–25]. But the direct contact with the TMDC results in, like in the case of ionic-gating, an entangled effect of charge redistribution and chemical hybridization [26], leading to non-universal, element-specific properties. Hence, an efficient method able to tune the chemical potential of TMDCs by large amounts without chemically altering it or leaving the surface inaccessible would be highly desirable. Such a method would make it possible to gain fundamental knowledge on the effect of charge on the band structure of TMDC semiconductors [13], ultimately enabling access to novel phases of matter, such as topological superconductivity [27].

Here, we introduce contactless chemical doping as a method to induce large shifts in the chemical potential of MoS_2, without disturbing its chemical environment. We chemically dope a Gr layer from below in order to shift the chemical potential of MoS_2 monolayer grown on top *in situ*. The doping is done through the use of intercalants, taking Eu and O as electron donor and acceptor respectively, to create high quality MoS_2/Gr/(Eu or O)/Ir(111) layered configurations. For both intercalants, it has been found that they are able to cause considerable shifts in the Dirac point of Gr (as far as $E_D = -1.38$ eV for Eu and up to $E_D = +0.68$ eV for O), without strong hybridization [28–31]. In this way, the chemical potential within the MoS_2 band structure can be controlled through the doping level of Gr and shifted far beyond what is possible in traditional back-gate device setups, without hybridization or loss of surface accessibility and quality. The MoS_2/doped Gr samples are analyzed experimentally with scanning tunneling microscopy (STM) and spectroscopy (STS) and theoretically with *ab initio* density functional theory (DFT) calculations. Additional attention is given to the effect of the Gr doping on the 1D states within mirror-twin boundaries (MTBs) in MoS_2, which can be filled and depleted via the substrate without compromising their 1D nature. Thereby, they can be used as chemical potential sensors.

1. Results

1.1. Metal–insulator transition in MoS_2

Our method is illustrated in figure 1(a). The initial heterostructure consists of three different materials: the 2D semiconductor MoS_2, the 2D semi-metal Gr, with the Dirac point close to Fermi level E_F, and the metallic Ir(111). Since foreign elements bind much more strongly to Ir(111) than to the van der Waals materials Gr and MoS_2, this arrangement enables us to intercalate these between Gr and Ir(111), while preserving the chemical environment of MoS_2. Here, the concept is demonstrated for the case of Eu and O. The applicability of our method to other 2D semiconductors is demonstrated in the SI (figure S1 available online at stacks.iop.org/TDM/9/025026/mmedia).

Concerning the choice of substrate, Gr is ideal as it fulfills the following requirements:

(a) It is a 2D material, creating the thinnest possible interface between MoS_2 and the intercalation layer.
(b) It has a low density of states (DOS) close to the Fermi energy, so large shifts of the band structure can be achieved with moderate carrier densities.
(c) Its work function is pinned to the band structure, i.e. energy shifts due to doping lead to equal shifts of the work function [32].
(d) The finite DOS allows for charge flow to MoS_2 when it becomes metallic.

Intercalating an electron donor such as Eu thus leads to an upward shift of the chemical potential in Gr via charge transfer. Similarly, the intercalation of an electron acceptor such as O causes the chemical potential of Gr to shift down in energy. These changes in the Gr substrate cause comparable shifts in the chemical potential of the top layer via workfunction alignment and/or charge transfer. The precise mechanisms by which the MoS_2 chemical potential is shifted for each intercalant will be discussed in detail below. In the following, we refer to MoS_2/Gr/Eu/Ir(111) (MoS_2/Gr/O/Ir(111)) as MoS_2 on n-doped (p-doped) Gr, while MoS_2/Gr/Ir(111) is refered to as pristine.

The STM topograph of figure 1(b) displays the pristine sample as a reference. Islands of monolayer (ML) MoS_2 are distributed on the Gr/Ir(111) substrate. The typical apparent height of the ML islands is 0.65 nm when tunneling into the MoS_2 conduction band. Apart from MTBs, which appear as bright lines, defects are largely absent. In the inset, an atomic resolution topograph of MoS_2 shows that the moiré of Gr/Ir(111) is visible through the MoS_2 layer, see SI (figure S2). This system has previously been investigated in detail in [5].

An STM image of MoS_2 on p-doped Gr is shown in figure 1(c). O was intercalated after the growth of MoS_2, as the O would etch Gr at the high temperatures employed in MoS_2 growth. The process is detailed in the section 3. The Gr layer is partially combusted, leaving uncovered areas (holes) in the graphene sheet, while the O atoms intercalate the subsisting Gr. An area where Gr was combusted is partly imaged in the top right of figure 1(c). After the process extended Gr patches remain, on which MoS_2 is found. The Gr layer is completely intercalated with a O-$(2\sqrt{3} \times 2\sqrt{3})$-R30° superstructure reported previously, see SI (figure S1) [33]. Since O-intercalation decouples Gr from Ir(111), the Gr/Ir(111) moiré

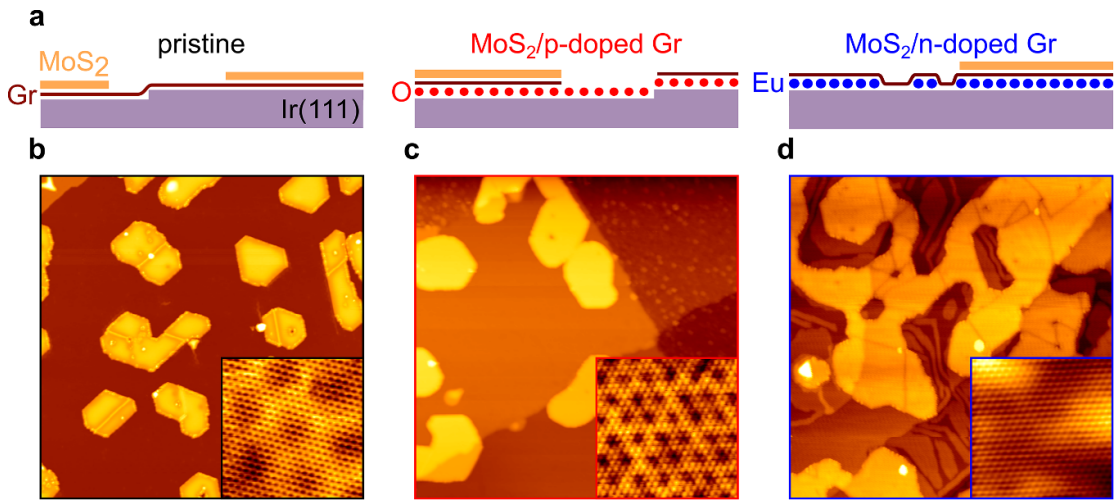

Figure 1. (a) Side view schematics visualizing the method of achieving large chemical potential shifts of MoS_2 on Gr/Ir(111). Left: pristine MoS_2. Middle: MoS_2 on p-doped Gr through post-growth O intercalation under Gr. Right: MoS_2 on n-doped Gr through pre-growth intercalation of Eu under Gr. (b)–(d) Constant current STM overview topographs of: (b) MoS_2/Gr/Ir(111); (c) MoS_2/Gr/O/Ir(111) and (d) MoS_2/Gr/Eu/Ir(111). (b) Sample sparsely covered by ML MoS_2. A single Ir(111) step edge is visible in the top left. The atomic resolution inset shows the moiré of Gr on Ir(111) imaged through the MoS_2. (c) Sample sparsely covered by ML MoS_2; no bilayers have formed. On the right, Ir(111) is not covered by Gr. The atomic resolution inset shows that the appearance of a MoS_2/Gr moiré. (d) Sample largely covered by ML MoS_2, with close to no bilayers present. Gr appears in two phases, bare (dark) and Eu-intercalated (brighter). As is highlighted by the inset, no Gr/Ir(111) moiré appears in the MoS_2 layer. STM parameters (V, I): (b) 1.0 V, 0.05 nA; (c) 3.5 V, 0.01 nA; (d) 1.0 V, 0.10 nA; (b)–(d) image size 150 × 150 nm^2. Insets: (b) 0.5 V, 0.58 nA; (c) 1.0 V, 0.10 nA; (d) 1.0 V, 0.10 nA; (b)–(d) image size 6.3 × 6.3 nm^2.

vanishes and a moiré between MoS_2 and Gr becomes visible as shown in the inset of figure 1(c).

Figure 1(d) is an STM topograph of the surface morphology of MoS_2 on n-doped Gr. The Gr layer not covered by MoS_2 is not uniformly intercalated: large intercalation areas and stripes of apparent height 0.30 nm are visible, similar to previous Gr/Eu/Ir(111) samples [34]. All investigated MoS_2 islands have an apparent height of around 0.70 nm relative to the higher (brighter in d) patches of Gr, under similar tunneling conditions as for the pristine sample, consistent with the absence of any Eu in between Gr and MoS_2. We thus infer that ML MoS_2 grows preferentially on top of Gr/Eu/Ir(111). A similar preference for adsorption on Eu-intercalated patches was observed for aromatic molecules [35]. The moiré of Gr/Ir(111) is no longer visible in the MoS_2 layer; instead, the layer shows slight apparent height modulations, due to a variation in the density of the intercalated Eu underneath Gr, see SI (figures S2 and S3).

We use STS to investigate how the band structure of MoS_2 is altered due to doping of the Gr substrate. The spectra in figures 2(a) and (b) are recorded in constant height and constant current mode on MoS_2, respectively. Constant height STS, in figure 2(a), is proportional to the local density of states and hence records the band gap position in energy. For pristine MoS_2 (black dots), the apparent valence band (VB) and conduction band (CB) edges are close to −1.8 eV and 0.9 eV, respectively. The doping of Gr leads to non-trivial energy shifts of these apparent band edges. The spectrum measured on MoS_2 on p-doped Gr displays a nearly rigid upward shift (≈450 meV)

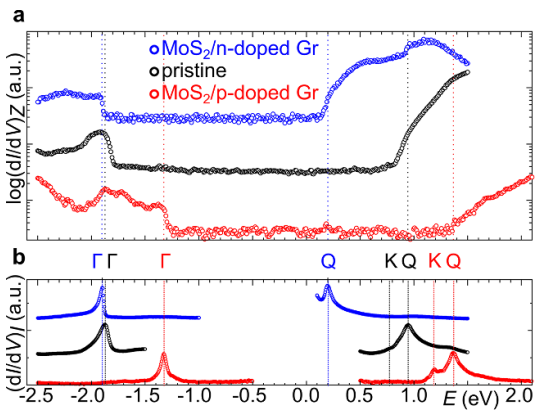

Figure 2. STS of ML MoS_2 on doped Gr, measured in (a) constant height and (b) constant current STS modes. MoS_2 on Gr/Ir(111) is shown in black; on Gr/O/Ir(111) in red; on Gr/Eu/Ir(111) in blue. The critical point energies are identified. The spectra have been shifted in dI/dV for visual clarity. STS parameters: (a) $V_{st} = 1.5$ V, $I_{st} = 0.2$ nA (black); 2.5 V, 0.5 nA (red); 1.5 V, 0.3 nA (blue); (b) $I_{st} =$ 0.1 nA (black); 0.1 nA (red); 0.2 nA (blue).

of the apparent VB and CB edges (red dots). Since both band edges shifted by approximately the same amount, the p-doping of Gr leaves the MoS_2 band gap nearly unchanged with only a minor reduction of ≈20 meV. Upon n-doping, a considerable narrowing of the band gap is found, with the apparent CB edge shifting close to the Fermi energy, while the apparent VB edge remains at approximately the same location (blue dots). The shift of the apparent CB by ≈700 meV demonstrates a large shift of the chemical potential of MoS_2, whereas the lack of

Table 1. Critical point energies (eV) identified in ML MoS_2 on different substrates using constant current STS (averaged over multiple data sets), and the corresponding distance between the well-defined Γ and Q peaks in STS $E_{\Gamma-Q}$. For more details on the MoS_2/Gr/Ir(111) data, including the determination of the actual electronic bandgap $E_g = 2.53$ eV, see [5]. The location of the K-point of MoS_2 on n-doped Gr has been determined using quasiparticle interference mapping (see figure 3), since it is not accessible via constant current STS.

MoS_2 on	Γ	K	Q	$E_{\Gamma-Q}$
Gr/Ir(111)	-1.87 ± 0.02	0.77 ± 0.02	0.90 ± 0.05	2.77 ± 0.05
Gr/Eu/Ir(111)	-1.90 ± 0.01	(-0.09 ± 0.01)	0.20 ± 0.01	2.10 ± 0.01
Gr/O/Ir(111)	-1.37 ± 0.04	1.22 ± 0.03	1.38 ± 0.03	2.75 ± 0.05

a significant shift of the apparent VB is indicative of a large band gap renormalization, as will be analyzed in more detail below.

Constant current STS detects the critical point energies in the band structure [5, 36]. It serves as a complementary method to constant height STS. The resulting spectra are shown in figure 2(b). We follow the analysis of [5] to identify the critical point energies of MoS_2. In the VB, the Γ-point band edge states cause a large peak [5], which is found in all three systems. The actual VB maximum at the K-point is not detected in MoS_2 because of its large parallel momentum, in-plane orbital character and close proximity in energy. Based on ARPES measurements, the VB K-point was estimated to lie 0.11 eV above the Γ-point energy of the VB [37, 38]. The CB minimum at the K-point, however, is dominated by out-of-plane orbitals and thus appears as a small shoulder [5, 39]. This shoulder is found in the pristine sample and in MoS_2 on p-doped Gr, but cannot be detected in MoS_2 on n-doped Gr with constant current STS, as the signal diverges near the Fermi energy. States from the CB Q-point edge cause a larger peak, which is reproducibly found in all three samples. For that reason, we specify the gap size $E_{\Gamma-Q}$, used for determining the renormalization energy, as the energetic distance between the well-defined VB Γ peak and the CB Q peak in constant current STS. The actual bandgap is expected to be at least 240 meV smaller, see [5]. The exact location of the critical point energies and estimated $E_{\Gamma-Q}$ gap sizes are listed in table 1.

Remarkably, we find that the CB of MoS_2 on n-doped Gr is effectively at the Fermi level. To address this point, we perform STS mapping to investigate the conduction band minimum (CBM) of MoS_2 on n-doped Gr. MoS_2 patches enclosed by grain boundaries and island edges host confined states, effectively forming a quantum well. Mapping these standing waves allows us to detect the quasiparticles close to the Fermi energy. Figure 3(a) displays STS maps of such a triangular quantum well, in which we identify quantized states [40]. The lowest state is pronounced already at −50 meV below the Fermi energy, providing the smoking gun for the metallic nature of MoS_2 on this substrate. In addition, more complex states appear at higher energies, as expected for an electron-like band.

Quasiparticle interference patterns around defects and confined quantum well states such as

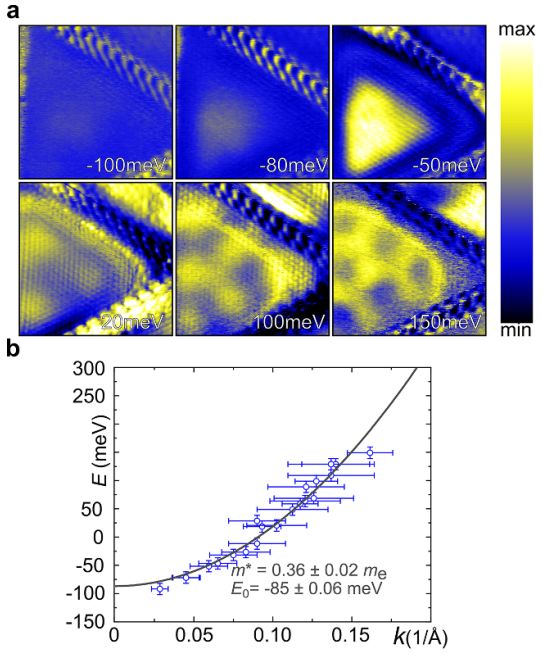

Figure 3. Metallic MoS_2 on Gr/Eu/Ir(111). (a) Six constant current differential conductance maps in an energy range of −100 meV to 150 meV with increasing energy. Imaged is a triangular quantum well formed by two MTBs and an island edge enclosing a small area of MoS_2. (b) Using multiple sets of STS maps, the dispersion of the electron-like conduction band near the K-point is plotted with a best parabolic fit. STM/STS parameters: (a) V_{st} as indicated, $I_{st} = 0.1$ nA, image size 9×9 nm^2.

those in figure 3(a) are used to determine the dispersion of the quasiparticles around the Fermi energy. The result is shown in figure 3(b). The different data sets and methods used to obtain these data points are shown and discussed in the SI (figure S4). We fit the data with a parabolic dispersion and find that the bottom of the band is located at -85 ± 6 meV. This is consistent with constant height STS measurements taken with small tip-sample distances, shown in the SI (figure S5). We further obtain an effective mass of 0.36 ± 0.02 m_e, which agrees with the calculated effective mass of 0.35–0.40 m_e at the K-point [41, 42].

1.2. DFT calculations and model of band shifts

We conducted DFT calculations to obtain a qualitative understanding of the mechanism through which the shifts of the chemical potential of MoS_2 are enabled. Our supercell includes the MoS_2 and Gr

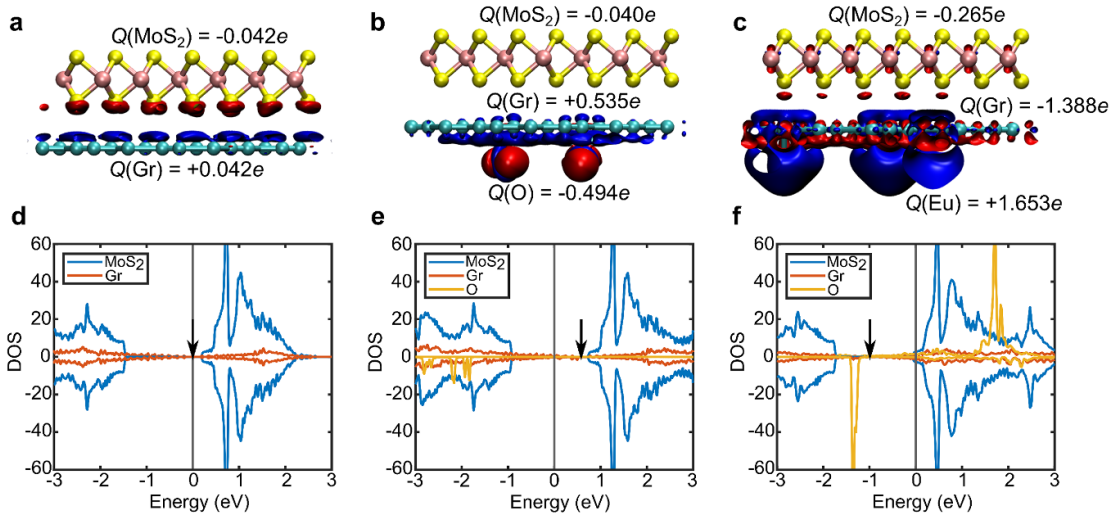

Figure 4. Density functional theory calculations of chemically gated MoS_2. Atomic structures of (a) MoS_2/Gr, (b) MoS_2/Gr/O and (c) MoS_2/Gr/Eu heterostructures. Q denotes the total charge (sum of Bader charges) in each of the constituent layers. The charge transfer is further visualized by the red and blue isosurfaces for increased and decreased electron density, respectively. The isosurface values are (a) 0.001 and (b), (c) 0.003 e Å^{-3}. (d)–(f) The corresponding local density of states. Positive and negative values refer to spin-up and -down components, respectively. Vertical black arrow denotes the position of the Gr Dirac-point. Fermi level is set to zero.

sheets, while the Ir(111) substrate was omitted. This simplified model of the experimental situation grasps the essentials at affordable computational effort. We also note that the renormalization of the fundamental bandgap due to screening is not accounted for in our DFT calculations. Since the band alignment is sensitive to strain in MoS_2 and Gr, we adopted a supercell model where strain was minimized.

Figures 4(a)–(c) show the structural models of the pristine heterostructure and the intercalated structures containing two O and two Eu dopants, respectively. The figures also show the total charge transfers, as obtained by summing up the Bader charges, and the charge density difference isosurfaces (defined as $\rho(MoS_2/Gr) - \rho(MoS_2) - \rho(Gr)$ and $\rho(MoS_2/Gr/dopants) - \rho(MoS_2/Gr) - \rho(dopants)$). In the case of the pristine heterostructure, the electronic structure at the interface is slightly perturbed by the presence of the other layers, which effectively yields a small charge transfer and an interface dipole induced potential shift of about 0.25 eV. In the case of the O-doped heterostructure, there is significant electron transfer from the Gr to O, while the MoS_2 layer is left mostly unaffected. This is in stark contrast to the Eu-doped heterostructure, where we find charge transfer from Eu to both Gr and MoS_2, albeit with the charge transfer to Gr still considerably larger. The charge transfer, induced dipoles and Dirac-point positions are listed in the SI (table S1).

Figures 4(d)–(f) show the DFT-calculated local densities of states projected onto the two or three constituent layers. We find that pristine MoS_2 is semiconducting, with the Fermi level 0.2 eV below CBM and the gap of 1.69 eV close to the value calculated for an isolated monolayer [43]. Gr remains charge neutral, with the Fermi level coinciding with the Dirac-point, since the interface dipole is the result of modifications to the extensions of the Gr wave functions and not of charge transfer. In the case of the O-doped heterostructure Gr is p-type doped, with the Fermi level 0.58 eV below the Dirac-point and 0.75 eV below the MoS_2 CBM. Thus we find a near-rigid shift of the Gr and MoS_2 bands to higher energies, in agreement to our experiments. In the case of the Eu-doped heterostructure Gr is n-type doped, with the Fermi level 0.99 eV above the Dirac-point and 0.05 eV above MoS_2 CBM. This represents a strong deviation from a rigid shift picture, in which one would expect the Fermi level to lie 0.8 eV above the MoS_2 CBM. DFT thus reproduces the metal–insulator transition, as well as the shifts of the Gr Dirac point and MoS_2 conduction band found experimentally, including deviations from a rigid shift. Our DFT model thus captures the essence of our experimental observations, although the absence of the Ir substrate leads to a significantly lower density of dopants needed to obtain shifts comparable to the experiments.

The physics involved in the changes of band edge positions and bandgap width can be grasped in a model, accounting for workfunction alignment and interface dipole formation, as shown in figures 5(a)–(c). The MoS_2, Gr and Ir(111) band diagrams are sketched for the three samples. Two interfaces are considered: between (doped) Gr and Ir(111), and between (doped) Gr and MoS_2. If charge transfer is possible between the layers (e.g. the metal–metal junction between Gr and Ir), an interface dipole will be formed, as a result of workfunction differences.

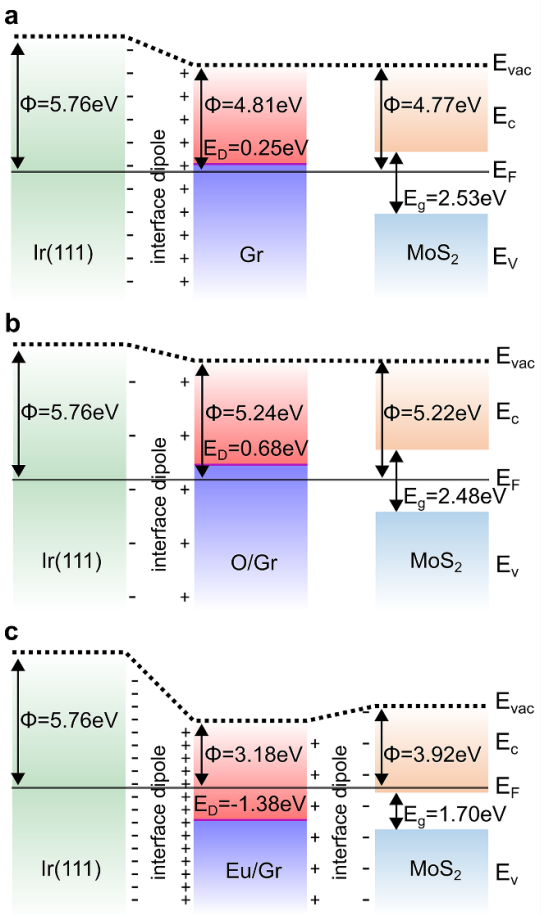

Figure 5. Band diagrams of MoS_2 on differently charged substrates. (a) MoS_2/Gr/Ir(111). (b) MoS_2/Gr/O/Ir(111). (c) MoS_2/Gr/Eu/Ir(111). Indicated are the vacuum level E_{vac}, the Fermi level E_F, the workfunctions Φ, the Gr Dirac point E_D and the MoS_2 conduction and valence bands E_C and E_V, respectively.

If no charge transfer is possible because one of the materials is gapped (e.g. the metal–semiconductor junction between undoped Gr and MoS_2), the workfunctions of the two materials have to align through shifts in the position of the chemical potential with respect to the band structure and thus to the vacuum level.

Both types of interfaces are present in the pristine case sketched in figure 5(a). The Ir(111) workfunction $\Phi_{Ir} = 5.76$ eV [44] is considerably larger than the workfunction of pristine Gr $\Phi_{Gr} = 4.56$ eV [45]. Due to the difference in workfunctions, charge will flow from Gr to Ir until an interface dipole is formed, halting the flow of further charge carriers. As a result, Gr is slightly p-doped when grown on Ir(111), by about 0.1 eV [46]. Note that for physisorbed Gr with an intact Dirac cone, e.g. Gr on Ir(111), even strong doping does not change the energetic separation of the Dirac point from the vacuum level, it being identical to the workfunction of undoped Gr [47].

When ML MoS_2 is placed on top of Gr, the interface dipole between Gr and Ir is marginally changed due to a slight increase in the p-doping of Gr, from +0.1 eV to +0.25 eV [37], resulting in a Gr workfunction 4.56 eV + 0.25 eV = 4.81 eV. Between the interior of the MoS_2 layer and Gr no charge transfer is possible, as the Fermi level lies within the MoS_2 band gap. Therefore, with no dipole formed, the workfunctions of both materials have to align. The chemical potential of MoS_2 correspondingly shifts from the middle of the band gap closer to the CB. With the ML MoS_2 electron affinity $\chi \approx 4.0$ eV [48–52], and finding the conduction band edge E_c of MoS_2/Gr/Ir(111) in STS at 0.77 eV, the workfunction of MoS_2 on Gr/Ir(111) $\Phi_{MoS_2} = \chi + E_{CBM} = 4.77$ eV is indeed very close to that of Gr: $\Phi_{Gr} = 4.81$ eV.

When O is intercalated underneath Gr, shown in figure 5(b), the Dirac point moves to 0.68 eV [31] and the Gr workfunction changes to 4.56 eV + 0.68 eV = 5.24 eV. The interface dipole between Gr and Ir(111) becomes smaller. Following the previous considerations, the MoS_2 bands must follow the shift of the Dirac point, in order to keep the workfunctions of Gr and MoS_2 the same. The measured K-point shift in the MoS_2 CB of ≈450 meV is correspondingly close to the expected Gr Dirac point shift of 430 meV. The chemical potential of MoS_2 is thus directly set by that of Gr, as long as MoS_2 remains insulating.

Experimentally, we find that the size of the band gap E_g is only slightly reduced, when comparing the p-doped and pristine sample. Since MoS_2 is still insulating, the screening within the layer should not have changed. Gr, on the other hand, has an increased hole density on the order of 10^{13} cm^{-2} due to an estimated Dirac point energy $E_D = -0.68$ eV [29]. Gr is thus expected to better screen electrostatic interactions in MoS_2. Previous experimental and theoretical work on TMDC/Gr heterostructures has however found that the effect of increased Gr carrier density on the band gap flattens off after $E_D = \pm 0.25$ eV [7, 53]. Since the Gr layer is already p-doped in the pristine MoS_2 sample [37], the observed renormalization of $\Delta E_g \approx 20$ meV seems to indicate that the substrate-induced renormalization is already close to saturation prior to O-intercalation.

For Eu-doped Gr, figure 5(c), the situation is decidedly different. Gr/Eu has its Dirac point at about −1.38 eV, see [28] and the SI (figure S6). The chemical potential difference between Eu-doped Gr and pristine MoS_2 is larger than the difference between pristine MoS_2 and the pristine CB edge. The MoS_2 potential will therefore shift in response to the Eu-doped Gr potential until it hits the CB and MoS_2 becomes metallic. Charge flows from Gr to MoS_2, creating an interface dipole, which reduces the shift of the MoS_2 CB minimum compared to the shift of the Dirac point of graphene.

In addition to the formation of an interface dipole, the charge carriers within MoS_2 are also able to efficiently screen within the layer, leading to the experimentally observed band gap reduction $\Delta E_g = 0.67$ eV. The renormalization of the bandgap

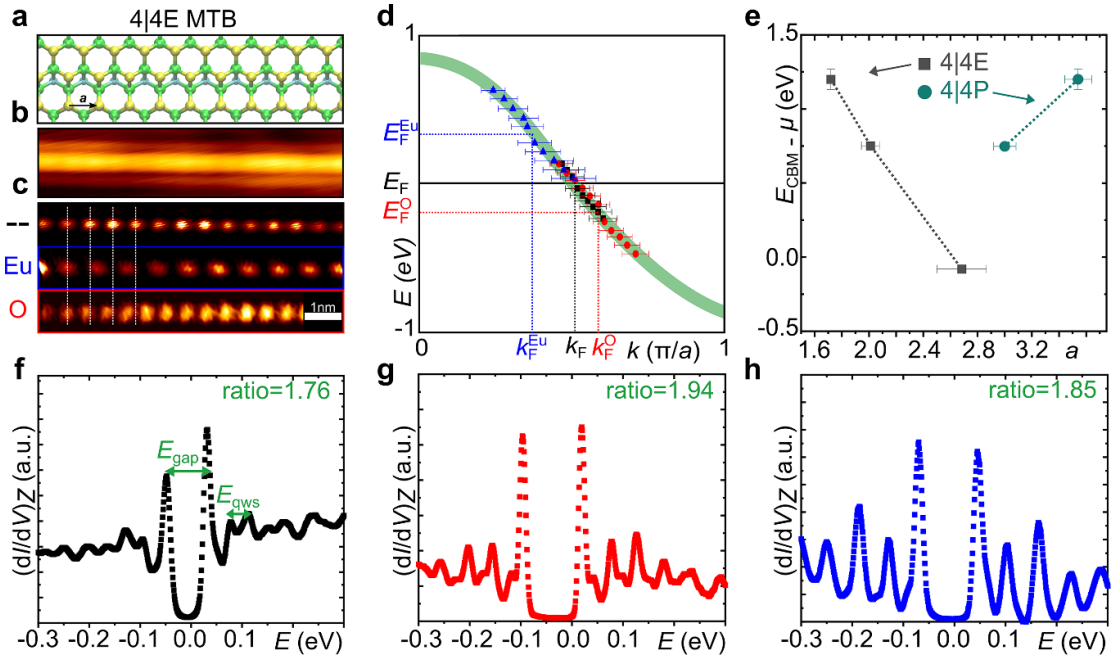

Figure 6. Confined states along 4|4E and 4|4P MTBs in ML MoS_2 on different substrates. (a) Ball-and-stick model of a 4|4E MTB. Mo atoms are navy, S atoms yellow (top layer) or dark yellow (bottom layer). A MoS_2 lattice vector is indicated. (b) Constant current STM topograph of a 4|4E MTB in MoS_2 on Gr/Ir(111). (c) Constant height STM image of a 4|4E MTB in pristine (–), p-shifted (O) and n-shifted (Eu) MoS_2. Vertical white lines are a guide to the eye. (d) Dispersion of the hole-like 1D band of the 4|4E MTB, with data from MTBs on the differently doped Gr substrates in their respective colors. In green a DFT-calculated dispersion for MoS_2/Gr/Ir(111) is shown, taken from [59]. Experimental data from spectra taken along the same MTBs as used for the averaged linescans in (f)–(h). (e) Plot of 4|4E (gray) and 4|4P (teal) MTB beating periodicity near E_F versus the location of the CBM. The dotted lines are a guide to the eye. (f)–(h) Constant height STS linescans along a 4|4E MTB in MoS_2/Gr/Ir(111) (left), MoS_2/Gr/O/Ir(111) (middle) and MoS_2/Gr/Eu/Ir(111) (right). The spectra are averaged over the whole length of the MTB. Indicated is the ratio of the gap at the Fermi level (E_{gap}) with respect to the average gap between the quantized states (E_{qws}). STM/STS parameters: (b) top panel: $V = 1.25$ V, $I = 0.02$ nA; (b) –: $V = 0.10$ V, $I_{st} = 0.5$ nA; O: $V = 0.02$ V, $I_{st} = 0.1$ nA; Eu: $V = 0.20$ V, $I_{st} = 0.05$ nA; 1 nm scale bar shown. (f) $V_{st} = 0.5$ V, $I_{st} = 0.1$ nA; (g) $V_{st} = 0.5$ V, $I_{st} = 0.1$ nA; (h) $V_{st} = -0.5$ V, $I_{st} = 0.1$ nA.

due to the metal–insulator transition is considerably larger than what is achieved via methods which only increase the carrier density in the substrate. In those cases, renormalization energies of at most 0.24 eV have been reported [7, 54].

1.3. Effect of charge on mirror twin boundaries

The presence of 0D defects (such as vacancies) or 1D defects (such as MTBs) in TMDCs will influence the shifts of the chemical potential induced via contactless chemical doping. In-gap states within these defects tend to weaken the impact of the work function difference due to local Fermi level pinning [55–57], which is absent away from these defects [58]. In the pristine sample, the presence of in-gap states below the Gr Fermi level in MoS_2 edges and MTBs leads to the accumulation of charge in the MTBs, causing band bending in the surrounding semiconductor [59]. With the doping of Gr potentially influencing the amount of charge that is transfered to the MTBs as well as the dielectric properties of the MoS_2/Gr heterostructure (e.g. by inducing a metal–insulator transition), it is worthwhile to disentangle the various effects of Gr doping on the MTB states and the electronic landscape surrounding them.

In MoS_2 two types of MTBs (4|4E and 4|4P) are present, formed between 180°-misoriented MoS_2 domains [60, 61]. A model and a constant currrent STM image of the 4|4E MTB are shown in figures 6(a) and (b), respectively. The 4|4P MTB is discussed in the SI (figure S4). In the pristine sample, the states within MTBs are strictly 1D, leading to strong electron-correlations and the emergence of Tomonaga–Luttinger liquid (TLL) behaviour [62]. In addition, since the states are located in boundaries of finite length, they are confined. Hence, when mapping the local density of states close to the Fermi energy, we expect a pronounced, sinusoidal beating pattern along the length of the MTB, resulting from quantized 1D electronic states, as shown in figure 6(c). The wavelength of this beating pattern is related to the confined states closest to the Fermi energy, $\lambda = \pi/k_F$ [62]. Therefore, if the charge donated by the Gr substrate shifts the Fermi level of the MTB band, the change in filling can be observed directly with STM, by imaging the periodicity of the states near E_F.

The constant height STM images in figure 6(c), taken near E_F, reveal the beating patterns found within 4|4E MTBs for MoS_2 on the differently doped substrates. In the pristine case, we find $\lambda_F^{Gr} = (2.01 \pm$

$0.04)\,a$ for the 4|4E MTBs, where $a = 0.315$ nm is the ML MoS_2 lattice constant [63]. For p-shifted MoS_2 the periodicity along the 4|4E MTBs has visibly decreased, $\lambda_F^O = (1.72 \pm 0.01)\,a$, while for n-shifted MoS_2, an increased periodicity of $\lambda_F^{Eu} = (2.69 \pm 0.11)\,a$ is measured.

The shifts in the beating periodicity can be understood from the band structure of the MTB. 4|4E MTBs host a hole-like band, which is shown in green in figure 6(d), based on DFT calculations discussed in [62]. With the Fermi level E_F in the pristine case bisecting the band at $k_F = \pi/2a$, this leads to the observed $2\,a$ periodicity. When the Gr substrate is n-doped, additional charge can flow into the boundary, raising the Fermi level to E_F^{Eu} and leading to an increased wavelength λ_F^{Eu}. For p-doping of Gr, the inverse happens: charge is extracted from the boundary, the Fermi level sinks to E_F^O and λ_F^O decreases. The quantitative relationship between k_F and the line charge in the boundary is given in the SI (table S2).

From the measured k values we find that the chemical potential shifts in the MTB are considerably smaller than those in Gr or MoS_2, with the Fermi level difference between the 4|4E on n- and p-doped Gr about 500 meV, see SI (table S2) for the exact values. In other words, the states within MTBs locally pin the Fermi level, while Fermi level pinning is absent in MoS_2 away from defects. This can be understood from previous considerations: the metal-metal interface between the MTB and Gr allows for charge transfer and thus the formation of an interface dipole. As a consequence, the MTB Fermi level will not shift as much as the chemical potential of MoS_2, which rigidly follows the Gr doping level until it becomes metallic. Note that the relation between λ_F and Fermi level is reversed for 4|4P MTBs, which host an electron-like band, see SI (figure S7).

Our findings are summarized in figure 6(e) in which we plot the position of the CBM of MoS_2 as a function of beating period for the two types of MTBs. This allows the identification of the Fermi wave vector of the MTB band and the position of the chemical potential μ with respect to the MoS_2 conduction band in a single STM image. Due to the close proximity of CBM and chemical potential in our n-shifted MoS_2 samples, we can also set a lower bound of $\lambda_F^{Eu} = (2.69 \pm 0.11)\,a$ for the beating pattern within 4|4E MTBs, for which the surrounding 2D material is metallic. As a consequence, the MTBs function as a sensor—they allow for a determination of the chemical potential of MoS_2 by measuring the periodicity of the MTB states near E_F. This method is also applicable at room temperature.

In figures 6(f)–(h) we display additional constant height STS linescans averaged along the length of 4|4E MTBs on all three substrates, respectively. The finite length of the MTBs leads to a series of peaks in the dI/dV spectra at the energetic location of the quantized states. The dominant lowest energy excitations for a given wavevector are used to obtain the dispersion within the 4|4E MTBs, see figure 6(d) [62]. We find a pronounced gap E_{gap} around the Fermi level, consistent with the presence of a Coulomb blockade which pushes the states closest to E_F further apart [62]. The gap is almost twice as large as the energy spacing between the quantized states E_{qws}. We find that the ratio E_{gap}/E_{qws}, which eliminates the length-dependence of both parameters [64], has only minor substrate-dependence. This is surprising, since the presence of a Coulomb gap, which arises from strong electron–electron interactions, indicates that the 1D correlated states within 4|4E MTBs persist even when the surrounding MoS_2 is metallic.

Moving away from the effects of the intercalation on the intrinsic MTB properties, we also investigated the region directly surrounding the boundaries, where the MoS_2 bands are bent under the influence of the MTB charge [59]. The magnitude of band bending must change if the amount of charge on the MTB is changed in consequence of Gr doping, while the shape of the bending provides insight into how the screening properties of MoS_2 are affected.

For reference, we take constant current STS linescans orthogonally crossing a 4|4E MTB in the pristine heterostructure. While figure 7(a) captures the behaviour of the CB edge, figure 7(b) captures that of the VB. Far away from the MTB, at $x = \pm 5$ nm, the unperturbed pristine band structure is observed. Approaching the MTB, located at $x = 0$ nm, both CB and VB are seen to bend upwards by at least 0.5 eV, indicating that the MTB is negatively charged. The bending is smooth in the CB but occurs stepwise at characteristic energies in the VB due to quantization effects [59].

On p-doped Gr, figures 7(c) and (d), the magnitude of the bending is severely reduced for both bands, while the spatial extent of the bending is similar to that of the pristine case. There are fewer quantized VB levels and the unperturbed band structure is recovered at $x = \pm 4$ nm. This can be understood from previous considerations: Gr is more p-doped, lowering its chemical potential. As a result, certain MTB states are now shifted above the Gr Fermi level and less charge can flow from Gr into the MTB, reflected in its smaller periodicity at E_F.

On n-doped Gr, shown in figures 7(e) and (f), the bending of the MoS_2 bands occurs in a much smaller range of $|2|$ nm on either side of the MTB. In figure 7(f) there are fewer quantized VB levels—only two—and their energy spacing is larger. The highest quantized state occurs at around -1.3 eV, compared to -1.0 eV found in the pristine sample. Additionally, the VB bends up steeply at $x \approx \pm 1.5$ nm from the boundary. The increase in band bending due to graphene n-doping is expected, as more charge is transferred into the MTB states.

The decrease of the spatial extent of band bending on the one hand is a sign of the metallic phase

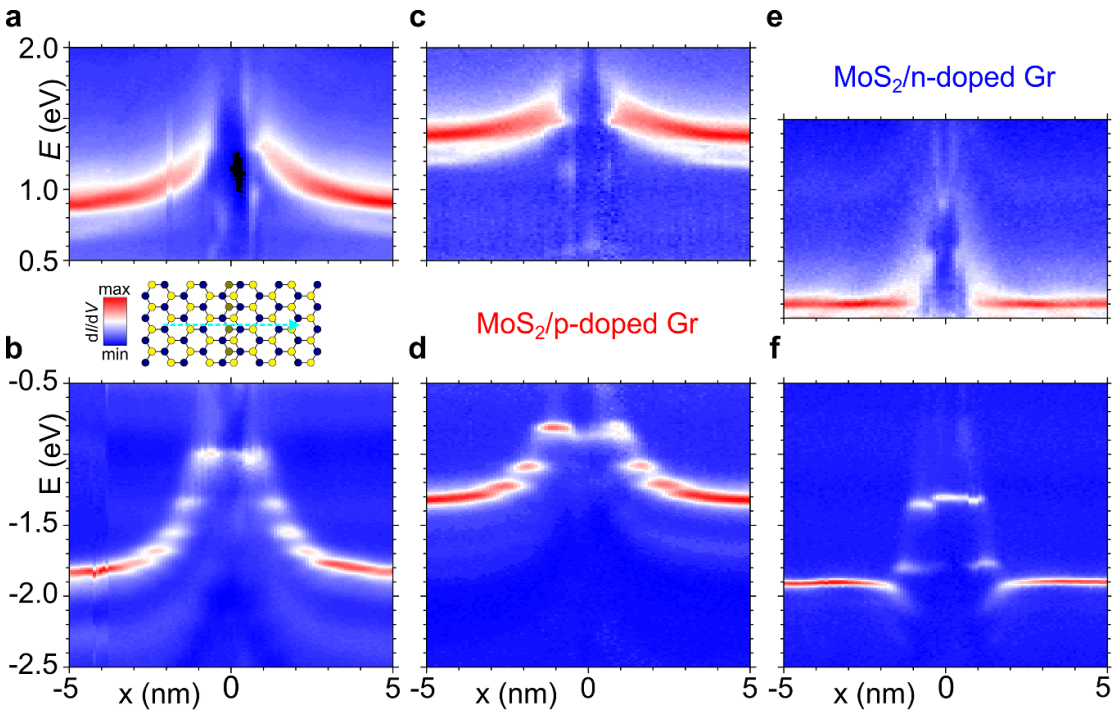

Figure 7. Band bending at 4|4E MTBs in ML MoS_2 on doped Gr: (a) and (b) on Gr/Ir(111); (c) and (d) on Gr/Eu/Ir(111); (e) and (f) on Gr/O/Ir(111). Constant current STS linescans are taken in the energy ranges of the CB (a), (c), (e) and VB (b), (d), (f) extrema. $(dI/dV)_I$ signals are plotted as a function of energy E and position x according to the color scale shown in (a), in arbitrary units. In a the path of a linescan over a 4|4E MTB model is shown, not to scale. STS parameters: (a) and (b) $V_{st} = \pm 2.5$ V, $I_{st} = 0.05$ nA; (c) and (d) $V_{st} = \pm 2.5$ V; (e) $V_{st} = 1.5$ V; (f) $V_{st} = -2.5$ V; (c)–(f) $I_{st} = 0.1$ nA.

of MoS_2 on Gr/Eu/Ir(111), which effectively screens the charge within the MTB. On the other hand, the steep band bending close to the MTB leaves the direct surrounding of the latter insulating, in line with the persistent Coulomb gap E_{gap} found experimentally.

2. Discussion

We have demonstrated a non-invasive method to strongly modify the electrostatic environment of ML MoS_2, applicable also to other TMDCs and van der Waals materials. We have shown that the doping of its Gr substrate can induce a metal–insulator transition in MoS_2 and enables the manipulation of metallic states within MTBs. In addition, the chemical potential shifts in MoS_2 can be monitored via MTB states and the screening environment around the boundaries. The backside functionalization of Gr leaves the TMDC top layer chemically pristine, thereby offering advantages over chemical doping or adatom techniques. Our contactless chemical doping method to shift the chemical potential of wide-bandgap semiconductors can be extended by other intercalants such as alkalis [65], other rare earth metals [66] or the p-dopant chlorine [67]. Continuous tuning of the chemical potential, analogous to gating, could be accomplished by using Li as intercalant [68, 69]. A combination of contactless gating for coarse adjustment of the chemical potential with electrostatic gating for fine adjustment represents another exciting perspective. As the conductive Gr substrate is not suited to most technological applications, replacing it with an insulating layer such as hexagonal boron nitride presents a promising approach to achieve practical implementation of this method. We envision that contactless chemical doping will enable observation and characterization of novel states of matter using both local and global surface science techniques.

3. Methods

The samples were grown *in situ* in a preparation chamber with base pressure $p < 5 \times 10^{-10}$ mbar. Ir(111) is cleaned by 1.5 keV Ar^+ ion erosion and annealing to temperatures $T \approx 1550$ K. Gr is grown on Ir(111) by two steps. First, room temperature ethylene exposure till saturation followed by 1370 K thermal decomposition gives well-oriented Gr islands. Second, exposure to 2000 l ethylene at 1370 K for 600 s yields a complete single-crystal Gr layer [70]. ML MoS_2 is grown by Mo deposition in an elemental S pressure of 1×10^{-8} mbar [71]. Subsequently, the sample is annealed to 1050 K in the same S background pressure. The Eu-intercalated sample is prepared in the order: Gr growth; Eu intercalation; MoS_2 growth. Eu is evaporated from a Knudsen cell onto the Gr/Ir(111) crystal kept at 720 K. Intercalation is confirmed by low-energy electron diffraction (LEED) [72]. After Eu intercalation no Eu is adsorbed on

Gr [72, 73]. Subsequently, the sample is annealed to 1075 K. Due to this annealing step, all Eu that could escape from underneath the Gr at the lower MoS_2 annealing temperature of 1050 K has already escaped. Thereby Eu contamination of MoS_2 during subsequent MoS_2 growth and annealing is prevented. The O-intercalated sample is prepared in the order: Gr growth; MoS_2 growth, O intercalation. O intercalation is achieved by exposing MoS_2/Gr/Ir(111) for 210 seconds at 770 K to 2×10^4 l of O_2 [30, 33]. No obvious increase in the density of point defects, such as oxygen substitutions [74], is observed in MoS_2 after oxygen intercalation.

STM and STS are carried out in the $T = 7$ K bath cryostat system after *in situ* transfer from the preparation chamber. STS is performed with the lock-in technique, at modulation frequency 619–777 Hz and modulation voltage $V_{\mathrm{mod}} = 4$ $\mathrm{mV_{rms}}$, with an experimental resolution of ≈10 meV or better [75]. We employ constant height (recording $(\mathrm{d}I/\mathrm{d}V)_Z$) and constant current ($(\mathrm{d}I/\mathrm{d}V)_I$) STS modes, where I is the tunneling current, V the bias voltage, and Z the tip-sample distance or height. In both modes $\mathrm{d}I/\mathrm{d}V$ is recorded while V is ramped; see [5] for further explanation. Spectra are always taken away (>6 nm) from defects, unless indicated otherwise.

All density functional theory calculations were carried out using the Vienna *Ab Initio* Simulation Package (VASP) [76, 77]. The plane wave cutoff was set to 400 eV throughout. We used the exchange-correlation functional of Perdew, Burke, and Ernzerhof (PBE) [78]. Van der Waals interactions are described using Grimme's semi-empirical corrections at the D2 level [79]. A 4 × 4 k-point mesh was used during structural optimization in the supercell, while the density of states is evaluated using a 16 × 16 mesh. The optimized lattice constants of MoS_2 and Gr are 3.18 Å and 2.468 Å, respectively. For a minimally strained heterostructure model, we used the same approach and model as in [39], wherein a 4 × 4 supercell of MoS_2 is interfaced with a $(6,3) \times (6,3)$ Gr cell (i.e. $\bar{a}_{\mathrm{sc}} = 6\bar{a} + 3\bar{b}$, where $\bar{a}$ and $\bar{b}$ are the lattice vectors of Gr at an 120° angle). The dopants were placed as far from each other as possible within the supercell. The optimized geometry for O atoms was between graphene top- and hollow-sites. The optimized geometry for Eu atoms was on the graphene hollow site.The MoS_2 layer is kept unstrained and Gr layer is compressively strained by 0.8%. Finally, in order to avoid the buckling of Gr due to chemical interactions with the dopants, charging, or strain, the z-coordinates of C atoms were fixed.

Data availability statement

The data that support the findings of this study are available upon reasonable request from the authors.

Acknowledgments

This work was funded by the Deutsche Forschungsgemeinschaft (DFG, German Research Foundation)—Project Number 277146847—CRC 1238 (Subprojects A01 and B06). Support from the German Academic Exchange Service DAAD and the Academy of Finland via PPP Finland MODEST, Project IDs 57458732 (DAAD) and 321914 (Academy of Finland) is gratefully acknowledged. The authors thank CSC IT Center for Science for the generous grants of computer time.

ORCID iDs

Camiel van Efferen https://orcid.org/0000-0002-6237-8602
Carsten Busse https://orcid.org/0000-0001-5522-0578
Hannu-Pekka Komsa https://orcid.org/0000-0002-0970-0957

References

[1] Xi X, Zhao L, Wang Z, Berger H, Forró L, Shan J and Mak K F 2015 Strongly enhanced charge-density-wave order in monolayer $NbSe_2$ *Nat. Nanotechnol.* **10** 765–9
[2] Chen Y *et al* 2020 Strong correlations and orbital texture in single-layer 1T-$TaSe_2$ *Nat. Phys.* **16** 218–24
[3] Ugeda M M *et al* 2016 Characterization of collective ground states in single-layer $NbSe_2$ *Nat. Phys.* **12** 92–97
[4] Li L, O'Farrell E, Loh K, Eda G, Özyilmaz B and Castro Neto A 2016 Controlling many-body states by the electric-field effect in a two-dimensional material *Nature* **529** 185–9
[5] Murray C, Jolie W, Fischer J A, Hall J, van Efferen C, Ehlen N, Grüneis A, Busse C and Michely T 2019 Comprehensive tunneling spectroscopy of quasifreestanding MoS_2 on graphene on Ir(111) *Phys. Rev.* B **99** 115434
[6] Nguyen P V *et al* 2019 Visualizing electrostatic gating effects in two-dimensional heterostructures *Nature* **572** 220–3
[7] Qiu Z *et al* 2019 Giant gate-tunable bandgap renormalization and excitonic effects in a 2D semiconductor *Sci. Adv.* **5** eaaw2347
[8] Ye J, Zhang Y J, Akashi R, Bahramy M S, Arita R and Iwasa Y 2012 Superconducting dome in a gate-tuned band insulator *Science* **338** 1193–6
[9] Lu J M, Zheliuk O, Leermakers I, Yuan N F, Zeitler U, Law K T and Ye J T 2015 Evidence for two-dimensional Ising superconductivity in gated MoS_2 *Science* **350** 1353–7
[10] Saito Y *et al* 2016 Superconductivity protected by spin–valley locking in ion-gated MoS_2 *Nat. Phys.* **12** 144–9
[11] Saito Y, Nojima T and Iwasa Y 2017 Highly crystalline 2D superconductors *Nat. Rev. Mater.* **2** 16094
[12] Lu J, Zheliuk O, Chen Q, Leermakers I, Hussey N E, Zeitler U and Ye J 2018 Full superconducting dome of strong Ising protection in gated monolayer WS_2 *Proc. Natl Acad. Sci.* **115** 3551–6
[13] Wang L *et al* 2020 Correlated electronic phases in twisted bilayer transition metal dichalcogenides *Nat. Mater.* **19** 861–6
[14] Ren Y, Yuan H, Wu X, Chen Z, Iwasa Y, Cui Y, Hwang H Y and Lai K 2015 Direct imaging of nanoscale conductance evolution in ion-gel-gated oxide transistors *Nano Lett.* **15** 4730–6
[15] Jo S, Costanzo D, Berger H and Morpurgo A F 2015 Electrostatically induced superconductivity at the surface of WS_2 *Nano Lett.* **15** 1197–202

[16] Costanzo D, Jo S, Berger H and Morpurgo A F 2016 Gate-induced superconductivity in atomically thin MoS_2 crystals *Nat. Nanotechnol.* **11** 339–44
[17] Fu Y *et al* 2017 Gated tuned superconductivity and phonon softening in monolayer and bilayer MoS_2 *npj Quantum Mater.* **2** 52
[18] Piatti E, De Fazio D, Daghero D, Tamalampudi S R, Yoon D, Ferrari A C and Gonnelli R S 2018 Multi-valley superconductivity in ion-gated MoS_2 layers *Nano Lett.* **18** 4821–30
[19] Costanzo D, Zhang H, Reddy B A, Berger H and Morpurgo A F 2018 Tunnelling spectroscopy of gate-induced superconductivity in MoS_2 *Nat. Nanotechnol.* **13** 483–8
[20] Helveg S, Lauritsen J V, Lægsgaard E, Stensgaard I, Njørskov J K, Clausen B S, Topsoe H and Besenbacher F 2000 Atomic-scale structure of single-layer MoS_2 nanoclusters *Phys. Rev. Lett.* **84** 951–4
[21] Alidoust N *et al* 2014 Observation of monolayer valence band spin-orbit effect and induced quantum well states in MoX_2 *Nat. Commun.* **5** 4673
[22] Zhang C, Johnson A, Hsu C-L, Li L-J and Shih C-K 2014 Direct imaging of band profile in single layer MoS_2 on graphite: quasiparticle energy gap, metallic edge states and edge band bending *Nano Lett.* **14** 2443–7
[23] Kang M *et al* 2017 Universal mechanism of band-gap engineering in transition-metal dichalcogenides *Nano Lett.* **17** 1610–5
[24] Katoch J *et al* 2018 Giant spin-splitting and gap renormalization driven by trions in single-layer WS_2/h-BN heterostructures *Nat. Phys.* **14** 355–9
[25] Liu H *et al* 2020 Spontaneous chemical functionalization via coordination of Au single atoms on monolayer MoS_2 *Sci. Adv.* **6** eabc9308
[26] Shao B, Eich A, Sanders C, Ngankeu A S, Bianchi M, Hofmann P, Khajetoorians A A and Wehling T O 2019 Pseudodoping of a metallic two-dimensional material by the supporting substrate *Nat. Commun.* **10** 180
[27] Hsu Y-T, Vaezi A, Fischer M H and Kim E-A 2017 Topological superconductivity in monolayer transition metal dichalcogenides *Nat. Commun.* **8** 14985
[28] Schumacher S *et al* 2013 The backside of graphene: manipulating adsorption by intercalation *Nano Lett.* **13** 5013–9
[29] Larciprete R *et al* 2012 Oxygen switching of the epitaxial graphene–metal interaction *ACS Nano* **6** 9551–8
[30] Grånäs E, Knudsen J, Schröder U A, Gerber T, Busse C, Arman M A, Schulte K, Andersen J N and Michely T 2012 Oxygen intercalation under graphene on Ir(111): energetics, kinetics and the role of graphene edges *ACS Nano* **6** 9951–63
[31] Jolie W, Craes F, Petrović M, Atodiresei N, Caciuc V, Blügel S, Kralj M, Michely T and Busse C 2014 Confinement of Dirac electrons in graphene quantum dots *Phys. Rev.* B **89** 155435
[32] Giovannetti G, Khomyakov P A, Brocks G, Karpan V M, van den Brink J and Kelly P J 2008 Doping graphene with metal contacts *Phys. Rev. Lett.* **101** 026803
[33] Martínez-Galera A J *et al* 2016 Oxygen orders differently under graphene: new superstructures on Ir(111) *Nanoscale* **8** 1932–43
[34] Schumacher S, Förster D, Rösner M, Wehling T and Michely T 2013 Strain in epitaxial graphene visualized by intercalation *Phys. Rev. Lett.* **110** 086111
[35] Huttmann F *et al* 2015 Tuning the van der Waals interaction of graphene with molecules via doping *Phys. Rev. Lett.* **115** 236101
[36] Zhang X *et al* 2015 Growth graphene on silver–copper nanoparticles by chemical vapor deposition for high-performance surface-enhanced Raman scattering *Appl. Surf. Sci.* **353** 63–70
[37] Ehlen N *et al* 2019 Narrow photoluminescence peak of epitaxial MoS_2 on graphene/Ir(111) *2D Mater.* **6** 011006
[38] Ehlen N 2017 private communication
[39] Komsa H-P and Krasheninnikov A V 2013 Electronic structures and optical properties of realistic transition metal dichalcogenide heterostructures from first principles *Phys. Rev.* B **88** 085318
[40] Li W-K and Blinder S M 1985 Solution of the Schrödinger equation for a particle in an equilateral triangle *J. Math. Phys.* **26** 2784–6
[41] Cheiwchanchamnangij T and Lambrecht W R L 2012 Quasiparticle band structure calculation of monolayer, bilayer and bulk MoS_2 *Phys. Rev.* B **85** 205302
[42] Qiu D Y, da Jornada F H and Louie S G 2013 Optical spectrum of MoS_2: many-body effects and diversity of exciton states *Phys. Rev. Lett.* **111** 216805
[43] Komsa H-P and Krasheninnikov A V 2015 Native defects in bulk and monolayer MoS_2 from first principles *Phys. Rev.* B **91** 125304
[44] Michaelson H B 1977 The work function of the elements and its periodicity *J. Appl. Phys.* **48** 4729–33
[45] Yan H, Sun Y, He L, Nie J-C and Chan M H W 2012 Observation of Landau-level-like quantization at 77 K along a strained-induced graphene ridge *Phys. Rev.* B **85** 035422
[46] Pletikosić I, Kralj M, Pervan P, Brako R, Coraux J, N'Diaye A T, Busse C and Michely T 2009 Dirac cones and minigaps for graphene on Ir(111) *Phys. Rev. Lett.* **102** 056808
[47] Khomyakov P A, Giovannetti G, Rusu P C, Brocks G, van den Brink J and Kelly P J 2009 First-principles study of the interaction and charge transfer between graphene and metals *Phys. Rev.* B **79** 195425
[48] Das S, Chen H-Y, Penumatcha A V and Appenzeller J 2013 High performance multilayer MoS_2 transistors with scandium contacts *Nano Lett.* **13** 100–5
[49] Lee S Y *et al* 2016 Large work function modulation of monolayer MoS_2 by ambient gases *ACS Nano* **10** 6100–7
[50] Hu C, Yuan C, Hong A, Guo M, Yu T and Luo X 2018 Work function variation of monolayer MoS_2 by nitrogen-doping *Appl. Phys. Lett.* **113** 041602
[51] Zhang C *et al* 2016 Systematic study of electronic structure and band alignment of monolayer transition metal dichalcogenides in van der Waals heterostructures *2D Mater.* **4** 015026
[52] Schlaf R, Lang O, Pettenkofer C and Jaegermann W 1999 Band lineup of layered semiconductor heterointerfaces prepared by van der Waals epitaxy: charge transfer correction term for the electron affinity rule *J. Appl. Phys.* **85** 2732
[53] Riis-Jensen A C, Lu J and Thygesen K S 2020 Electrically controlled dielectric band gap engineering in a two-dimensional semiconductor *Phys. Rev.* B **101** 121110
[54] Ugeda M M *et al* 2014 Giant bandgap renormalization and excitonic effects in a monolayer transition metal dichalcogenide semiconductor *Nat. Mater.* **13** 1091–5
[55] Allain A, Kang J, Banerjee K and Kis A 2015 Electrical contacts to two-dimensional semiconductors *Nat. Mater.* **14** 1195–205
[56] Diaz H C, Ma Y, Chaghi R and Batzill M 2016 High density of (pseudo) periodic twin-grain boundaries in molecular beam epitaxy-grown van der Waals heterostructure: $MoTe_2$/MoS_2 *Appl. Phys. Lett.* **108** 191606
[57] Bampoulis P, van Bremen R, Yao Q, Poelsema B, Zandvliet H J W and Sotthewes K 2017 Defect dominated charge transport and Fermi level pinning in MoS_2/metal contacts *ACS Appl. Mater. Interfaces* **9** 19278–86
[58] Le Quang T, Cherkez V, Nogajewski K, Potemski M, Dau M T, Jamet M, Mallet P and Veuillen J-Y 2017 Scanning tunneling spectroscopy of van der Waals graphene/semiconductor interfaces: absence of Fermi level pinning *2D Mater.* **4** 035019
[59] Murray C, van Efferen C, Jolie W, Fischer J A, Hall J, Rosch A, Krasheninnikov A V, Komsa H-P and Michely T 2020 Band bending and valence band quantization at line defects in MoS_2 *ACS Nano* **14** 9176–87
[60] Zou X, Liu Y and Yakobson B I 2013 Predicting dislocations and grain boundaries in two-dimensional metal-disulfides from the first principles *Nano Lett.* **13** 253–8

[61] Komsa H-P and Krasheninnikov A V 2017 Engineering the electronic properties of two-dimensional transition metal dichalcogenides by introducing mirror twin boundaries *Adv. Electron. Mater.* **3** 1600468
[62] Jolie W *et al* 2019 Tomonaga–Luttinger liquid in a box: electrons confined within MoS_2 mirror-twin boundaries *Phys. Rev.* X **9** 011055
[63] Kormányos A, Burkard G, Gmitra M, Fabian J, Zólyomi V, Drummond N D and Fal'ko V 2015 $\mathbf{k}\cdot\mathbf{p}$ theory for two-dimensional transition metal dichalcogenide semiconductors *2D Mater.* **2** 022001
[64] Yang X *et al* 2021 Manipulating Hubbard-type Coulomb blockade effect of metallic wires embedded in an insulator (arXiv:2104.08577)
[65] Petrović M *et al* 2013 The mechanism of caesium intercalation of graphene *Nat. Commun.* **4** 2772
[66] Klimovskikh I, Krivenkov M, Varykhalov A, Estyunin D and Shikin A 2019 Reconstructed Fermi surface in graphene on Ir(111) by Gd-Ir surface alloying *Carbon* **147** 182–6
[67] Vinogradov N A, Simonov K, Generalov A, Vinogradov A, Vyalikh D, Laubschat C, Mårtensson N and Preobrajenski A 2012 Controllable p-doping of graphene on Ir (111) by chlorination with $FeCl_3$ *J. Phys.: Condens. Matter* **24** 314202
[68] Schröder U A *et al* 2016 Core level shifts of intercalated graphene *2D Mater.* **4** 015013
[69] Halle J, Néel N and Kröger J 2016 Filling the gap: Li-intercalated graphene on Ir(111) *J. Phys. Chem.* C **120** 5067–73
[70] Coraux J *et al* 2009 Growth of graphene on Ir(111) *New J. Phys.* **11** 023006
[71] Hall J, Pielić B, Murray C, Jolie W, Wekking T, Busse C, Kralj M and Michely T 2018 Molecular beam epitaxy of quasi-freestanding transition metal disulphide monolayers on van der Waals substrates: a growth study *2D Mater.* **5** 025005
[72] Schumacher S *et al* 2014 Europium underneath graphene on Ir(111): intercalation mechanism, magnetism and band structure *Phys. Rev.* B **90** 235437
[73] Schumacher S, Förster D F, Rösner M, Wehling T O and Michely T 2013 Strain in epitaxial graphene visualized by intercalation *Phys. Rev. Lett.* **110** 086111
[74] Barja S *et al* 2019 Identifying substitutional oxygen as a prolific point defect in monolayer transition metal dichalcogenides *Nat. Commun.* **10** 1–8
[75] Morgenstern M 2003 Probing the local density of states of dilute electron systems in different dimensions *Surf. Rev. Lett.* **10** 933–62
[76] Kresse G and Furthmüller J 1996 Efficient iterative schemes for *ab initio* total-energy calculations using a plane-wave basis set *Phys. Rev.* B **54** 11169–86
[77] Kresse G and Furthmüller J 1996 Efficiency of *ab-initio* total energy calculations for metals and semiconductors using a plane-wave basis set *Comput. Mater. Sci.* **6** 15–50
[78] Perdew J P, Burke K and Ernzerhof M 1996 Generalized gradient approximation made simple *Phys. Rev. Lett.* **77** 3865
[79] Grimme S 2006 Semiempirical GGA-type density functional constructed with a long-range dispersion correction *J. Comput. Chem.* **27** 1787